A PARAMETRIC STUDY ON GRAIN STRUCTURE IN SELECTIVE LASER MELTING PROCESS FOR STAINLESS STEEL 316L

Dongwei Sun, Xuxiao Li, and Wenda Tan
Department of Mechanical Engineering, The University of Utah, Salt Lake City, UT 84112

Abstract

Laser Selective Melting (SLM) process is used in this work to produce 3-dimensional samples of Stainless Steel (SS) 316L. The effects of laser power, scanning speed, and laser scanning strategy on the track morphology and grain structure are investigated. As the laser heat input is increased by increasing laser power and/or decreasing laser scanning speed, the surface morphology of the SLM track will vary according to the extent of powder melting, and the grain size will increase correspondingly. Different laser scanning strategies can produce different grain patterns, and a noticeable porosity can be found if the scanning strategy is not appropriate. The grains in the bottom layers of the built samples inherit the crystallographic orientations from the substrate through epitaxial growth; nucleation takes places in the top layers and introduces new grains of random crystallographic orientations into the built samples.

Keywords: Selective laser melting, stainless steel 316L, deposition track morphology, grain structure.

1. Introduction

Additive Manufacturing (AM), which is opposed to subtractive manufacturing, has gathered much interest from both industry and academia in the past years [1]. It is a process to manufacturing 3-Dimensional (3D) objects from CAD models by slicing models into layers and adding materials into the product in a layer-upon-layer manner. Selective Laser Melting (SLM) is an important AM process, especially for metallic materials. It utilizes a laser energy source to build parts via selectively melting the metallic powder bed in a layer-wise mode [2]. Despite various advantages for metal AM, SLM still suffers from strong microstructure and property anisotropy, among other challenges [3, 4]. The material anisotropy in SLM is primarily caused by the layer-upon-layer nature of the AM processes, which introduces numerous interfaces between adjacent layers that reduce the material homogeneity along the building direction [5-7].

Stainless steel (SS) 316L is one of the most widely investigated materials for SLM, due to its broad applications [8, 9]. For the SLM of stainless steel, the microstructure and properties of the built objects may vary with different processing parameters, including laser energy input, hatch space, scanning strategies, and powder properties, etc. The combination of various processing parameters generates complex thermal history in the objects, which affect the macro-scale track morphology and geometry as well as the microstructure [3].

In this work, an in-house SLM system was established. Different laser power, scanning speed, and scanning strategies were used in the experiments to fabricate single-track samples as well as samples with multiple tracks and multiple layers. The effects of the processing parameters on track morphology and grain structure were investigated.

2. Materials and experiments

2.1 Materials

The SS316L powders were acquired from *Atlantic Equipment Engineers* with the chemical composition as shown in Table 1. The mean diameter and density of the powders were -325 mesh (44 μm) and 7.9 G/cm^3, respectively. Fig. 1 shows the typical morphology of SS316L powders observed using a scanning electron microscope (SEM).

Table 1: Chemical composition (in wt%) of SS316L powder

Fe	Cr	Ni	Mo
70	16-18	10-14	2-3

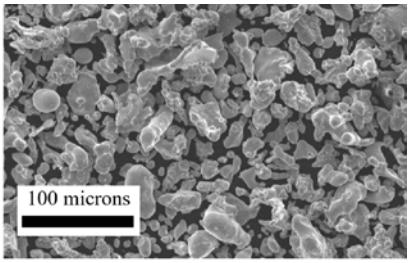

Fig. 1: SEM image of SS316L powder

2.2 Experiment Setup

An in-house developed system as shown in Fig. 2 was used for the experiments in this work. The system consists of a 500 Watt Continuous Wave Yb fiber laser (by IPG Photonics®) and a 2-Dimensional Laser Scanning Galvo Mirror System (GVSM002/M, by Thorlab®). An SS316L substrate was placed on a vertical motor stage. A layer of SS316L powders of 200 μm thickness was spread over the substrate. Experiments were conducted with different laser powers, scanning speeds, and scanning strategies. Argon gas was used to avoid molten pool oxidation.

Fig. 2: In-house developed Selective Laser Melting system.

2.3 Experiment Design

To investigate the effects of laser parameters and scanning strategies on grain growth behavior, experiments were conducted to produce samples with a single track and with multiple tracks and multiple layers. A wide range of laser power and scanning speed was used in the single-track experiments to identify the appropriate parameter window for the fabrication of multi-track and multi-layer samples. For the multi-track and multi-layer experiments, different laser scanning strategies were used. As shown in Fig. 3a, the laser always scans with a zigzag pattern in each layer, and the laser scanning direction of the first track (shown by red arrows) in the layer is used to denote the laser scanning direction in that entire layer, which can be along +X, –X, +Y, and –Y direction. For the example case in Fig. 3b, the laser scans along the +X direction in the first (black) layer; then switch 180° to be along -X direction in the second (green) layer; the laser then scans along +X direction in the third (red) layer, and along –X direction in the fourth (blue) layer. This scanning strategy is denoted as +X-Y+X-X. The other scanning strategies, following the same notation rules, are denoted as +X+X+X+X, +X+Y+X+Y, +X+Y–X–Y.

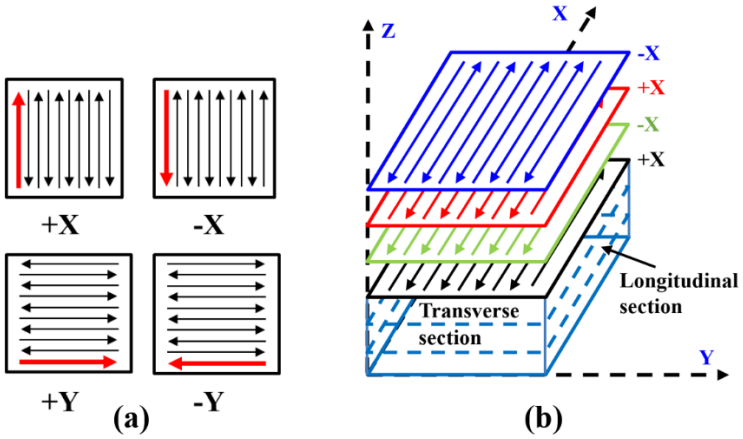

Fig. 3: Schematics of (a) scanning direction in each layer and (b) scanning strategy across multiple layers.

2.4 Characterization

The as-built SS316L samples were cut and polished for metallographic characterizations. The samples were chemically etched for 6 minutes with an etchant consisted of HNO_3 (5 mL), HCl (15 mL) and distilled water (20 mL). Surface morphology and microstructure were observed using an Optical Microscope (OM), and Electron Back-Scatter Diffraction (EBSD) was used to characterize the grain texture in the samples.

3. Results and discussion

3.1 Macrostructure

A series of single-track experiments were conducted within a power range of 100~400 W and a scanning speed range of 8~106 mm/s. The macro-scale morphology and geometry of the deposition tracks, including their continuity, height, and width, were investigated. According to

the surface morphology of the tracks (see Fig. 4a), the samples were categorized into 4 types with the corresponding parameter window shown in Fig. 4c.

1) Slight Melting: With a low laser power and a high scanning speed, insufficient laser heat input was delivered to the powder bed. Only a small amount of powders were melted, and the balling phenomenon was found to be significant for the melted metal (see the top view in Fig. 4a). Moreover, the laser barely penetrated the powder bed and reach the substrate, and hence the bonding between the track and substrate was rather weak (see the cross-section in Fig. 4b).

2) Discontinuous Melting: As the laser heat input was enhanced by increasing the laser power and/or decreasing the scanning speed, the melting of the powder bed was improved. While the molten tracks were still unstable and discontinuous, less balling phenomenon and longer tracks were found. Moreover, noticeable melting of the substrate was achieved.

3) Moderate Melting: In the range with appropriate laser power and scanning speed, the laser heat input was sufficient to melt through the power bed and penetrate into the substrate. The molten track was continuous with a smooth surface and a stable geometry (width and height). Moderate melting is considered the best scenario in the parameter ranges in this study.

4) Excessive Melting: As the laser scanning speed was further reduced, excessive heat input was available to create very wide and deep molten pools. Cracks can be found on the top surface of the track.

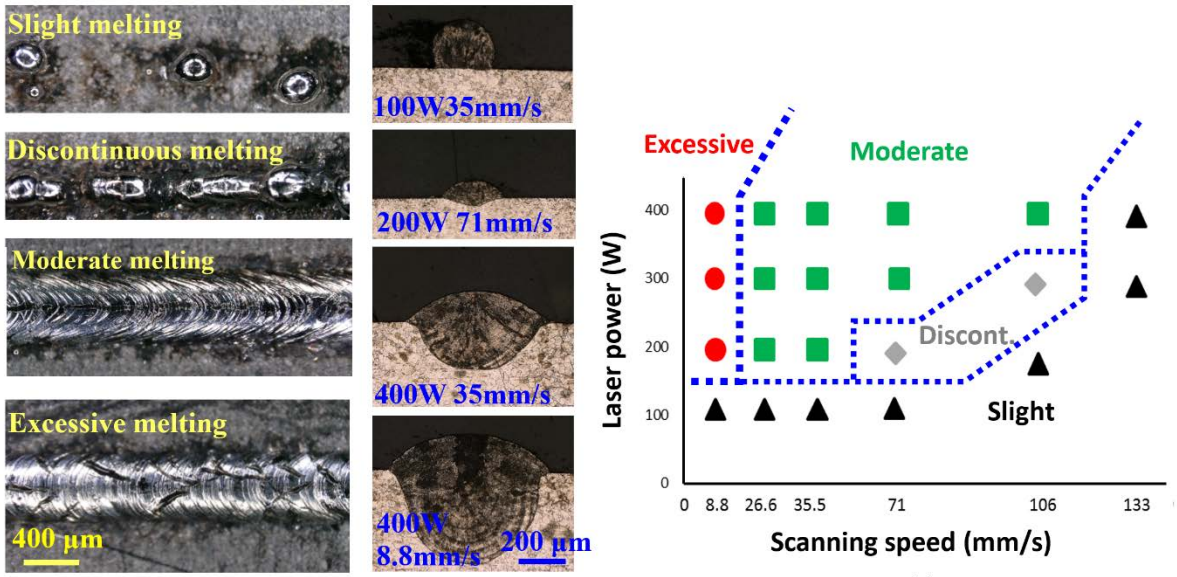

Fig. 4: Images of deposition tracks: (a) from top view, (b) from cross-section view, and (c) the melting status as functions of processing parameters.

The width and depth of the tracks were measured from their cross-sections (see Fig. 4b) and are plotted in Fig. 5. Both width and depth have shown a decreasing trend as the laser scanning speed is increased and/or the laser power is decreased.

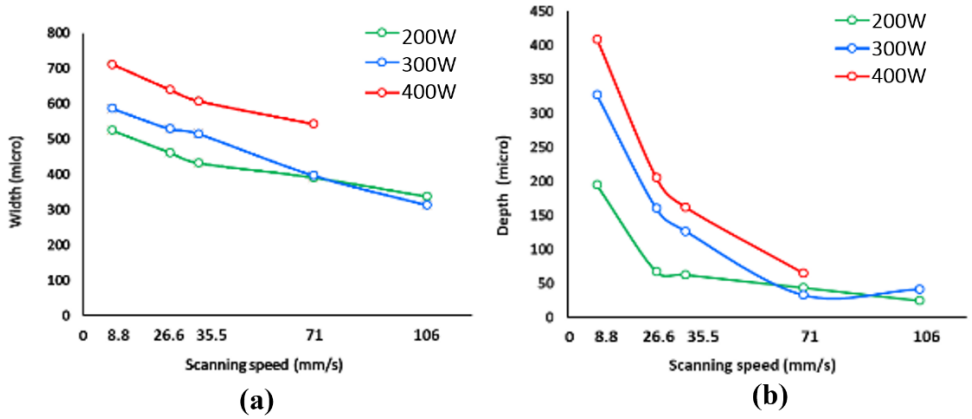

Fig. 5: Effects of laser power and scanning speed on (a) track width and (b) track depth.

Multi-track and multi-layer experiments were then conducted to build samples. The laser parameters were fixed at a laser power of 200 W and a scanning speed of 26.6 mm/s, and 4 different scanning strategies, namely +X+X+X+X, +X-X+X-X, +X+Y+X+Y, and +X+Y-X-Y, were used in the experiments. Even with the same laser power and scanning speed, different scanning strategies can generate different thermal histories, which pose noticeable effects on the porosity of the built objects. It can be found from Fig. 6 that irregular pores were randomly dispersed throughout the cross-section of the samples built with +X+X+X+X and +X-X+X-X scanning strategies, while few pores could be found in the samples built with the strategies of +X+Y+X+Y and +X+Y-X-Y. The possible reason is schematically shown in Fig. 7. With the first two scanning strategies (as shown in Fig. 7a), the tracks in all the layers are parallel to each other. The overlap regions between different tracks and different layers (as marked out by the blue starts), where the lack-of-fusion pores are most likely generated, will be piled up along the +Z direction. In the last two scanning strategies (as shown in Fig. 7b), the tracks in the second layer are perpendicular to the tracks in the first layer, and can re-melt the lack-of-fusion pores in the first layer (if there are any). This significantly helps to reduce and even remove the pores in the built objects [12, 13].

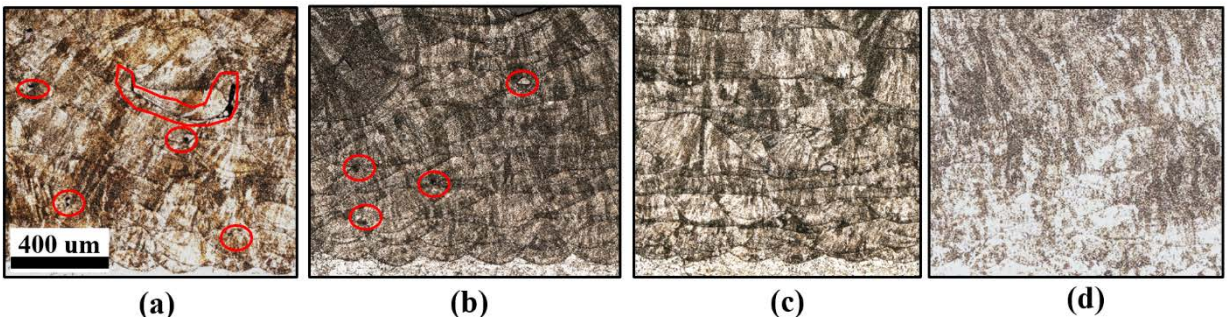

Fig. 6: Optical images of samples fabricated by different scanning strategies: (a) +X+X+X+X, (b) +X-X+X-X, (c) +X+Y+X+Y, and (d) +X+Y-X-Y. Red circles mark out pores.

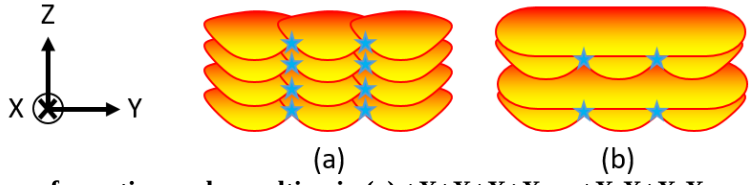

Fig. 7: Schematics of pore formation and remelting in (a) +X+X+X+X or +X-X+X-X scanning strategies and (b) X+Y+X+Y and +X+Y-X-Y strategies.

3.2 Microstructure

The grain structure in the substrate was first analyzed. Fig. 8a shows the Inverse Pole Figure (IPF) orientation mapping of the substrate. The color key for all the orientation mapping in this work is given in Fig. 8b. The IPF of the substrate is also given in Fig. 8c.

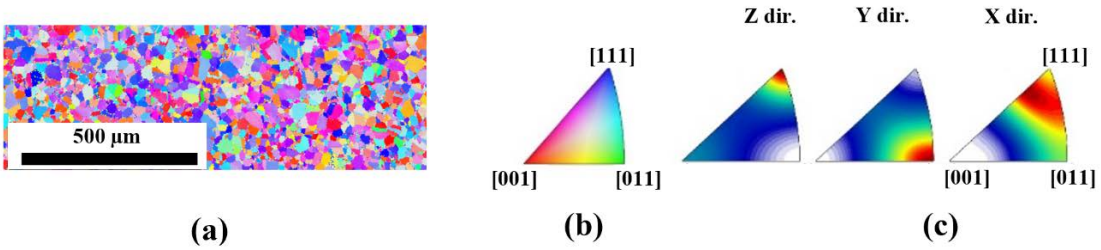

Fig. 8 (a) Inverse pole figure orientation mapping of substrate; (b) color key; and (c) inverse pole figure of substrate.

The grain textures of single-track samples were then analyzed. Fig. 9 shows the EBSD results for a series of samples fabricated with the same laser power but different scanning speeds. With an increase of scanning speed and hence a decrease of laser heat input, the size of the tracks on their cross-sections is reduced. The columnar grains are very obvious in Fig. 9a, while the grains seem to be equi-axed in Fig. 9b-9d. However, the IPFs of the 4 cases all show very similar patterns to that of the substrate (see Fig. 8c), which suggests that the grains in all the 4 cases have the very similar Crystallographic Orientations (COs). One reasonable explanation is that in all these 4 cases, the grains in the deposition tracks inherit the COs from the substrate, which is most likely due to the epitaxial growth from the partially melted grain on the fusion line [10,14]. The "equi-axed" grains in Fig. 9b-9d are likely the sections of columnar grains that grow from the fusion line.

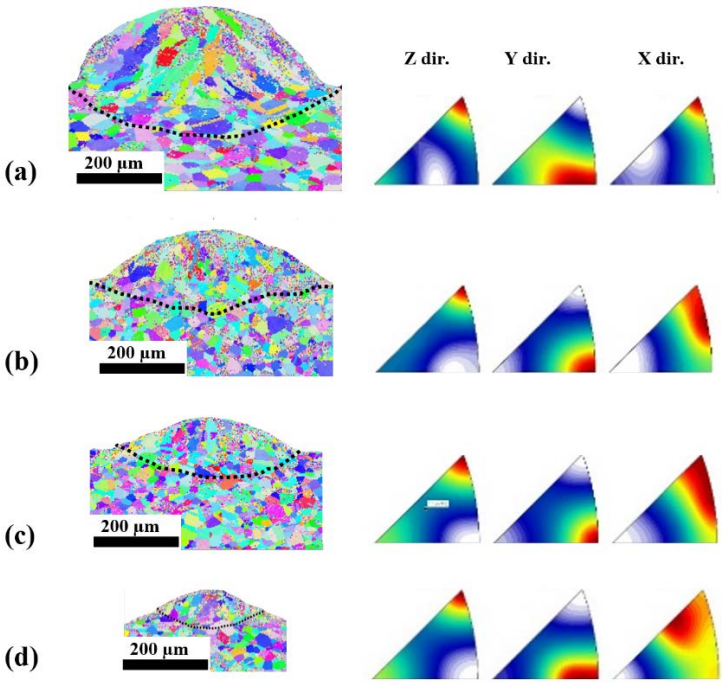

Fig. 9: Inverse pole figure orientation mapping (left) and inverse pole figure (right) for deposition tracks of P=200W and (a) V=8.8 mm/s, (b) 26 mm/s, (c) 35 mm/s, (d) 71 mm/s.

The average grain size in the deposition tracks was estimated from the EBSD results, and is plotted for cases of different laser power and scanning speed in Fig. 10. The plot shows a noticeable decrease in grain size as the laser power is decreased or the scanning speed is increased.

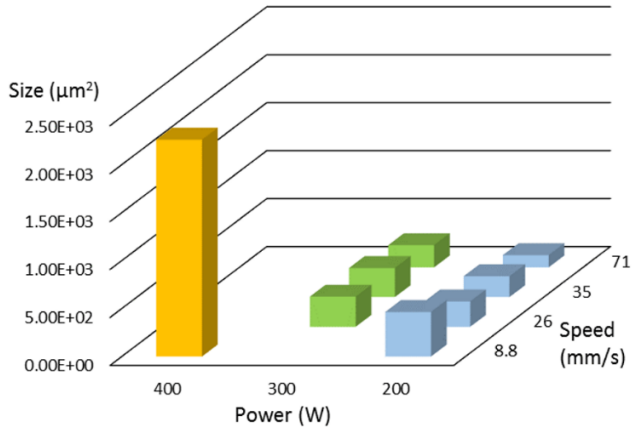

Fig. 10: Grain size as functions of laser power and scanning speed.

The grain texture in the multi-track and multi-layer samples were also investigated. Shown in Fig. 11 are the EBSD results on both the longitudinal section and cross-section of the sample built with the +X-X+X-X strategy. Columnar grains were found to prevail in both sections. On the longitudinal section (see Fig. 11a), three regions are marked out, region A in the substrate, region B in the bottom layers, and region C in the top layers. It was found that the IPFs in the bottom layers is similar to that of the substrate, which suggests that the grains in the bottom layers have inherited the COs from the substrate through the mechanism of epitaxial growth. However, the IPF in the top layers is quite different from that in the substrate and bottom layers. This implies that additional nucleation events occurred and introduced new grains with random COs into the built object. This phenomenon is confirmed in the cross-section in Fig. 11b: the IPFs are similar in the substrate (region D) and bottom layers (region E), but different in the top layers (region F).

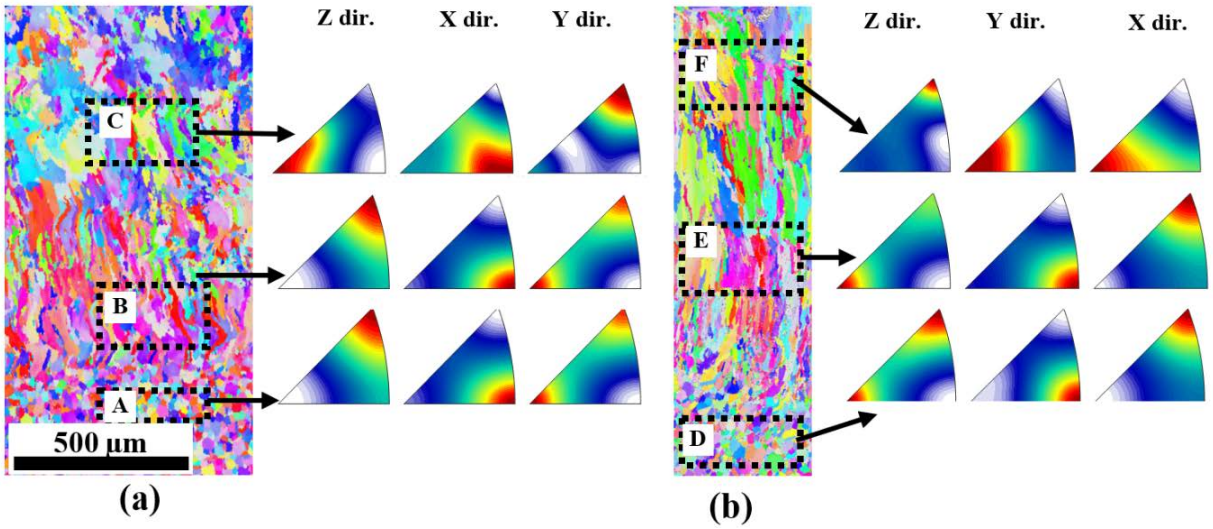

Fig. 11: Inverse pole figure orientation mapping (left) and inverse pole figure (right) for (a) longitudinal section (b) cross-section of +X-X+X-X sample.

EBSD observations were also conducted for the samples fabricated with other laser scanning strategies. Shown in Fig. 12 is the results for the sample of +X+Y-X-Y, which is the most complex scanning strategy in this study. Due to the switch of laser scanning direction between different layers, a clear layered pattern was found. Also, the IPFs in the substrate (region A) was similar to that in the bottom layers (region B), while the two regions in the top layers (region C and D) both have unique orientation patterns in their IPFs.

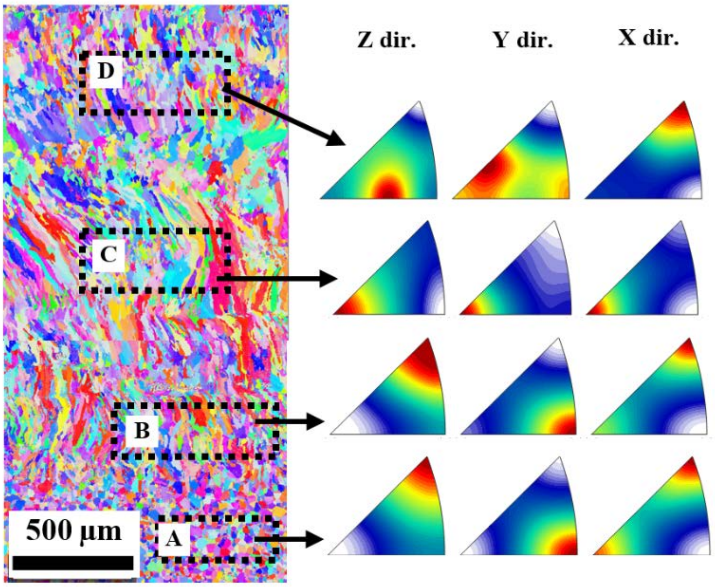

Fig. 12: Inverse pole figure orientation mapping (left) and inverse pole figure (right) for a longitudinal section of +X+Y-X-Y sample.

4. Conclusion

The major goal of the present work was to investigate the grain growth behavior and texture of SS316L manufactured by SLM under different parameters. The key findings are summarized as follows:

(1) As the laser power is increased or the scanning speed is decreased, the laser heat input is enhanced. Different types of melting are identified according to characteristics of topography and cross section, such as (1) insufficient melting, (2) slight melting, (3) moderate melting, and (4) excessive melting.

(2) The laser scanning strategy has a direct effect on the porosity of the built objects: the strategies with the perpendicular scanning directions between two adjacent layers help to remelt and remove the existing pores.

(3) Noticeable grain refinement can be found if the laser heat input is increased by increasing laser power or decreasing scanning speed.

(4) The EBSD results suggest that the grains in the bottom layers of the built samples inherit the crystallographic orientations from the substrate through epitaxial growth; nucleation takes place and introduces grains of new crystallographic orientations into the top layers of the built samples.

While some preliminary investigations have been conducted to study the effects of SLM parameters, including laser power, scanning speed, and scanning strategy on the grain size and orientation. Further quantitative analyses of the grain texture as well as the in-grain dendrite morphology will be carried out in the future work.

Reference

[1] Gibson, I., Rosen, D.W. and Stucker, B., 2010. *Additive manufacturing technologies*. New York: Springer.

[2] Frazier, W.E., 2014. Metal additive manufacturing: a review. *Journal of Materials Engineering and Performance*, *23*(6), pp.1917-1928.

[3] de Lima, M.S.F. and Sankaré, S., 2014. Microstructure and mechanical behavior of laser additive manufactured AISI 316 stainless steel stringers. *Materials & Design*, *55*, pp.526-532.

[4] Hanzl, P., Zetek, M., Bakša, T. and Kroupa, T., 2015. The influence of processing parameters on the mechanical properties of SLM parts. *Procedia Engineering*, *100*, pp.1405-1413.

[5] Dai, D. and Gu, D., 2014. Thermal behavior and densification mechanism during selective laser melting of copper matrix composites: simulation and experiments. *Materials & Design*, *55*, pp.482-491.

[6] Zhang, Q., Chen, J., Guo, P., Tan, H., Lin, X. and Huang, W., 2015. Texture and microstructure characterization in laser additive manufactured Ti–6Al–2Zr–2Sn–3Mo–1.5 Cr–2Nb titanium alloy. *Materials & Design*, *88*, pp.550-557.

[7] Lin, X., Yang, H., Chen, J. and Huang, W., 2006. Microstructure evolution of 316L stainless steel during laser rapid forming. *Acta Metallurgica Sinica-Chinese Edition*, *42*(4), pp.361.

[8] Miranda, G., Faria, S., Bartolomeu, F., Pinto, E., Madeira, S., Mateus, A., Carreira, P., Alves, N., Silva, F.S. and Carvalho, O., 2016. Predictive models for physical and mechanical properties of 316L stainless steel produced by selective laser melting. *Materials Science and Engineering: A*, *657*, pp.43-56.

[9] Dewidar, M.M., Khalil, K.A. and Lim, J.K., 2007. Processing and mechanical properties of porous 316L stainless steel for biomedical applications. *Transactions of Nonferrous Metals Society of China*, *17*(3), pp.468-473.

[10] Lampman, S. ed., 1997. *Weld integrity and performance: a source book adapted from ASM international handbooks, conference proceedings, and technical books*. ASM International.

[11] Zhang, D.Q., Liu, Z.H. and Chua, C.K., 2013,. Investigation on forming process of copper alloys via Selective Laser Melting. In *High Value Manufacturing: Advanced Research in Virtual and Rapid Prototyping: Proceedings of the 6th International Conference on Advanced Research in Virtual and Rapid Prototyping, Leiria, Portugal,* pp. 285.

[12] Li, R., Liu, J., Shi, Y., Wang, L. and Jiang, W., 2012. Balling behavior of stainless steel and nickel powder during selective laser melting process. *The International Journal of Advanced Manufacturing Technology*, *59*(9-12), pp.1025-1035.

[13] Kruth, J.P., Froyen, L., Van Vaerenbergh, J., Mercelis, P., Rombouts, M. and Lauwers, B., 2004. Selective laser melting of iron-based powder. *Journal of Materials Processing Technology*, *149*(1), pp.616-622.

[14] Nelson, T.W., Lippold, J.C. and Mills, M.J., 2000. Nature and evolution of the fusion boundary in ferritic-austenitic dissimilar metal welds. Part 2-On-cooling transformations. *Welding Research*, (10), pp.267-277.